Kakade, Rohan and Walker, John G. and Phillips, Andrew J. (2015) Optimising performance of a confocal fluorescence microscope with a differential pinhole. Measurement Science and Technology, 27 (1). ISSN 1361-6501

Optimising performance of a confocal fluorescence microscope with a differential pinhole

Rohan Kakade*, John G. Walker and Andrew J. Phillips

Advanced Optics Group, Faculty of Engineering, The University of Nottingham, University Park, Nottingham NG72RD, UK
**Corresponding author: Rohan Kakade (eexrk7@nottingham.ac.uk)*

The signal-to-noise ratio (SNR)-resolution trade-off is of great importance to bio-imaging applications where the aim is to image the sample using as little light as possible without significantly sacrificing image quality. In this paper the inherent SNR-resolution tradeoff in Confocal Fluorescence Microscopy (CFM) systems is presented by means of an effective tradeoff curve. A CFM system that employs a differential pinhole detection scheme has recently been shown to offer increased resolution, but at the expense of SNR. An optimum profile for the differential pinhole is identified in this paper that offers improved performance over a conventional (circular pinhole) system. The performance enhancement is illustrated through computer simulation.

1. Introduction

Abbe wave theory predicts that, for an aberration-free optical microscope, the achievable resolution is limited to approximately half the illumination wavelength [1]. Although decreasing the illumination wavelength improves the resolution, microscopy is largely undertaken in the visible spectra both for convenience and to avoid the shorter wavelengths causing radiation damage to the sample. Because of these problems and the requirement of sample fixation [2] electron microscopy has proved unsuitable for live cell studies. With the ability to tag virtually every molecular protein [3], fluorescence microscopy has become an indispensable tool in microbiology. Even with improvements in quality of optical elements [4], aberration correcting optics [5], large numerical apertures and no optical misalignments, the resolution is still limited to ~200nm in the lateral and ~500nm in the axial direction [6].

Advances in fluorescence microscopy, however have demonstrated techniques that surpass this resolution limit. 4Pi and image interference microscopy (I^5M) [7] are two interference type techniques that offer high axial resolution but no lateral improvement. 4Pi microscopy employs a second objective to produce a more spherical illumination pattern that results in an enhanced axial resolution of ~90nm [7]. I^5M, which achieves ~100nm axial resolution, uses the same principle as 4pi but in a widefield setup, and offers no lateral resolution gain [8]. Another method based on structured-light standing-wave fluorescence microscopy (SWFM) [9] uses all the excitation light as an axially varying standing wave to achieve similar axial resolution gains. Gains in the lateral direction were realised using techniques such as structured illumination microscopy (SIM) [10], lateral modulated excitation microscopy [11] and harmonic excitation light microscopy (HELM) [12]. HELM microscopy improves lateral as well as axial resolution to ~100nm [12, 13] by creating high-frequency fringes using four beams interfering in the sample. Studying even thicker samples was made possible using certain non-linear methods. Scanning photoelectron microscopy (SPEM) is one such method which excites higher order harmonics into the illumination structure by saturating the excited state of the fluorophores yielding a resolution in the 50-60nm range [14]. A far-field technique, stimulated emission depletion microscopy (STED) has been demonstrated to yield an axial resolution of ~30nm [8]. Amongst the near-field techniques is near-field scanning optical microscopy (NSOM) which is capable of offering lateral resolution of ~20nm [8] when studying samples in close proximity (<10nm). NSOM achieves this by measuring near-field evanescent waves [15] using a probe close to the sample surface, discounting thereby the need for focusing using lenses. Single molecule localization based methods such as photo-activated localization microscopy (PALM) and stochastic optical reconstruction microscopy (STORM) have been shown to offer resolutions of ~20-30nm in the lateral direction and ~50nm in the axial direction [16]. However PALM and STORM require long exposure times and this limits their use in live-cell imaging. The principal drawback of all these techniques is the cost and complexity of their implementation as well as the extensive computational reconstruction that is often required.

When evaluating the performance of a microscope both the signal-to-noise ratio (SNR) and resolution need to be taken into consideration. The impact of one on the other is very apparent in confocal fluorescence microscopy (CFM) in which the SNR- resolution

tradeoff is of great significance as fluorophores are vulnerable to photobleaching [17] and toxic cell damage [18]. In comparison to widefield fluorescence microscopy (WFM), CFM is more expensive and complex, but is widely used owing to its optical sectioning capability. CFM achieves this through its use of a detection pinhole, which by rejecting light away from the focal plane, makes optical sectioning possible. The lateral resolution in CFM improves by a factor $\sim\sqrt{2}$ over WFM.

A small confocal pinhole, by limiting the number of photons reaching the detector, reduces the SNR but improves resolution by narrowing the mainlobe and reducing sidelobes of the CFM point spread function (PSF). For a CFM system with a given set of illumination and detection pupils the shape of the lateral point spread function is significantly influenced by the pinhole geometry (see equation 1). By adjusting the pinhole to permit only the central peak viz., the infocus light, lateral resolution improvement is realised. Thus, the pinhole size, as well as its geometry, plays an important role in determining the resolving power and also the SNR of the system.

In this paper we investigate the use of an alternative pinhole geometry in CFM. This involves detecting two signals one from a central circular pinhole and the other from an annular region around the central region; this we designate as a 'differential' pinhole. The idea of using a differential pinhole has been discussed by various authors [19-22]. In references [19-21], physical pinholes are suggested, whereas in reference [22] the same concept is suggested but using a CCD detector array to emulate the pinholes. Segawa, Kozawa and Sato [23] discuss subtractive techniques for more general dual PSF microscopes, but the implementation of these is more complex requiring special polarised illumination.

The aim of this paper is to investigate the effect of varying the parameters describing a differential pinhole on resolution and SNR. Optimum parameters are identified and it is shown that the signal resulting from this design provides a significantly improved SNR-resolution trade-off than the circular pinhole used in existing CFM systems.

The organisation of the paper is as follows. The physical setup and key analytical expressions for SNR and resolution calculation are detailed in section 2. The impact of the differential pinhole on system performance is investigated in section 3. Section 4 presents computer-simulation results obtained using an optimum pinhole geometry.

2. CFM imaging and the SNR-Resolution trade-off

Consider an object illuminated by a lens (point spread function $\boldsymbol{PSF_1}$) of a CFM system being imaged onto a detection plane using a detection lens (point spread function $\boldsymbol{PSF_2}$). A detector is placed just after a pinhole in this plane with transmittance $\boldsymbol{Pin(v)}$. For this system the 3D point spread function $\boldsymbol{PSF}$ is given by,

$$PSF(v,u) = PSF_1(v,u)\big(\, PSF_2(v,u) * Pin(v)\big) \tag{1}$$

Here v and u are optical radial and optical axial coordinates related to object radial displacement r and object defocus z by equations (2) and (3) [24].

$$v = k\, r \sin\alpha \tag{2}$$

$$u = k\, z \sin^2\alpha \tag{3}$$

where $\boldsymbol{\alpha}$ is the lens semi-aperture angle, $\boldsymbol{\lambda}$ is the illumination wavelength and $\boldsymbol{k = 2\pi/\lambda}$. For a lens with pupil $\boldsymbol{P}$ the 3D lens PSF intensity in polar coridinates for a small $\boldsymbol{\alpha}$ is given by [25, 26].

$$PSF_{lens}(v,u) = \left| 2\pi \int_0^1 P(\rho) \exp\left(-\frac{ju\rho^2}{2}\right) J_0(v\rho)\rho \, d\rho \right|^2 \tag{4}$$

Here $\sin\alpha \approx a/f$ is the numerical aperture of either lens where a is the pupil radius, f is the focal length (assumed equal for both lenses under unity magnification). This is a good approximation if $f \gg a \gg \lambda$ and $a^2/\lambda f \gg 1$ [25]. The final image is given by the convolution of the object fluorescence intensity with the system PSF[27]. We make the assumption throughout that the excitation and emission wavelengths are equal. For a particular 3D object with fluorophore concentration $O(v,u)$, the image $I(v,u)$ is then given by the 3D convolution ($*$),

$$I(v,u) = O(v,u) * PSF(v,u) \tag{5}$$

The lateral resolution may be determined by computing the full-width half maximum (FWHM) of the PSF along the lateral direction. The axial resolution is computed by measuring the FWHM of the response of the system to a planar object as it is moved in the axial direction.

Amongst the various noise sources that degrade the signal quality in a CFM, shot noise has been acknowledged to be dominant in bio-imaging [28]. It is well known that the photon distribution is Poissonian. Thus, the mean and variance of the distribution are equal and the SNR can be readily calculated as the ratio of the mean number of detected photons (determined at the image plane) to standard deviation. We determine a normalised version of the SNR for a planar uniform object of unity fluorescence in the focal plane and for this case it reduces to the expression in equation(6), which has a maximum value of unity for a large detector pinhole.

$$SNR = \frac{\text{mean detected photons}}{\sqrt{\text{mean detected photons}}} = \sqrt{\int 2\pi \, PSF(v,u=0)dv} \tag{6}$$

Figure 1 shows plots of SNR vs resolution in both axial and lateral directions calculated for a conventional circular pinhole. The curves characterise the SNR-resolution trade-off as the pinhole radius is varied.

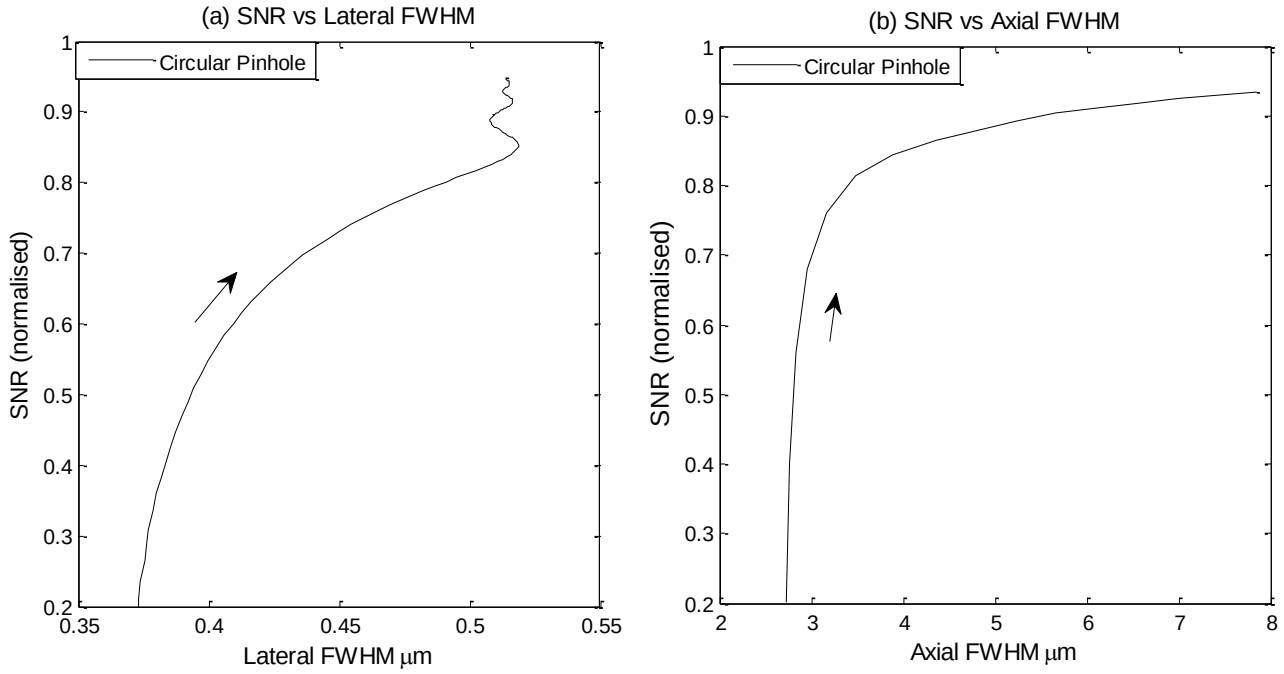

Figure 1. SNR-Resolution trade-off in the (a) lateral and (b) axial directions for a conventional circular pinhole as the pinhole radius is varied. The arrows indicate the direction of increasing pinhole radius; NA = 0.5 and **λ**= 0.5μm

Pinhole size and geometry play an important role in deciding the performance of a CFM system. Applications demanding a high SNR would require a large pinhole and this would invariably impede resolution. As can be seen from equation (1) the pinhole function directly affects the shape of the 3D PSF and experimenting with other pinhole shapes might offer a better SNR-resolution trade-off. In the next section we introduce the concept of a differential pinhole – an alternative pinhole arrangement that brings this about.

3. A Differential Pinhole

Consider an elliptical shaped pinhole (figure 2(b)) tilted an angle of 45 degrees as seen in figure 2(a) whose projection in the plane perpendicular to the optical axis (see figure (2(c)) assumes a circular shape defined mathematically by equation (7).

$$Pin(r) = \begin{cases} 1 & \text{for } r < r_i \\ -\gamma & \text{for } r_i < r < r_p \\ 0 & \text{elsewhere} \end{cases} \tag{7}$$

where r_p is the pinhole radius, r_i is the radius of the inner transparent annuli and γ is the multiplication factor applied to the photon counts from the second detector. Note that a similar output would be achieved by using a reduced reflectivity for the outer annulus but this would give an inferior SNR in the subtracted signal.

This detector arrangement could be implemented practically as shown in figure 2(a) by allowing different parts of the light onto separate detectors. Notably this arrangement requires two detectors (i.e. increased system cost) and the 45 degree tilt of the design would cause the different sides of the pinhole to be in slightly different planes. An alternative approach to overcome the above problems would be to employ a detector array and to sum appropriate pixels in a similar way to the arrangement in [22]. This detector array approach has the advantage that many different pinhole sizes and regions used for image formation may be selected from a single measurement. The

advantage of the detector approach shown in figure 2(a) is that fast and high dynamic range detectors such as PMT's may be used. For confocal applications, such as fluorescence lifetime imaging microscopy (FLIM) or fluorescence (cross-) correlation spectroscopy (FCS/FCCS), that demand very high speed data acquisition, point detectors such as PMTs prove more suitable than CCDs [29]. Expanding on the ideas laid down by Bertero [30] and Sheppard[31], ZEISS recently introduced the LSM 880 microscope that employs the so called Airyscan detector [32]; 32 individual detector elements functioning as pinholes capture all available light from an Airy disk simultaneously. At the expense of a slightly increased implementation cost (from the use of a reflective pinhole and two point detectors), the detector arrangement in figure 2, can offer similar data acquisition speeds to a conventional CFM.

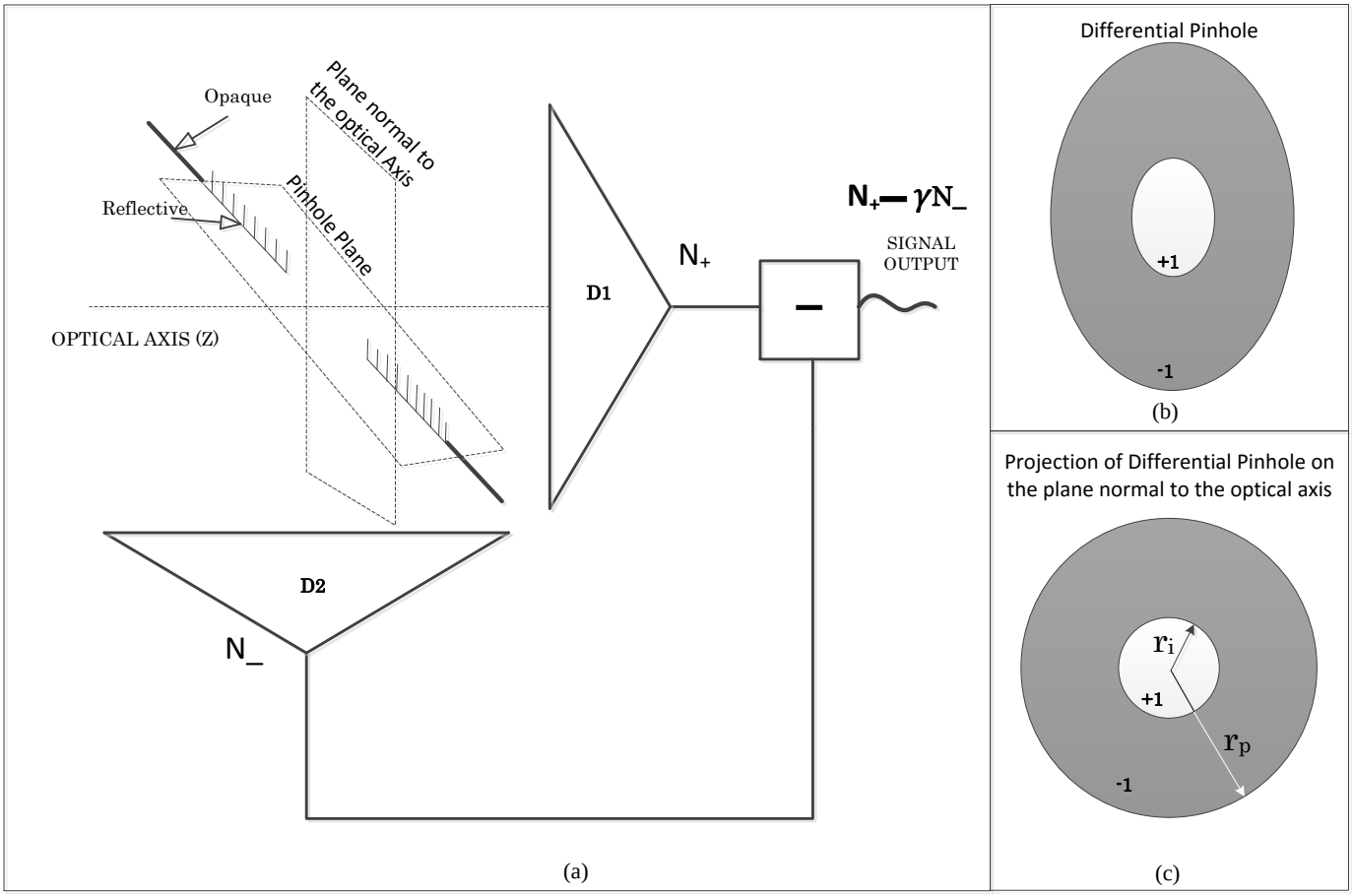

Figure 2. (a) Detector arrangement showing how a differential pinhole is realised using two detectors D1 and D2. (b) The Differential pinhole. (c) The pinhole's projection on a plane perpendicular to the optical axis is shown. D1 collects the photons incident within a pinhole radius $\mathbf{r_i}$ while D2 detects photons reflected within the region $r_i < r < r_p$. The photon counts are subtracted to produce the final signal.

If N_+ and N_- denote the number of photons collected by detectors D1 and D2 respectively then the received signal S is given by $N_+ - \gamma N_-$ and the total noise variance by the sum of the noise variances generated by D1 and D2 (see equation 8). Thus the SNR of a CFM system using a differential pinhole is given by equation (9).

$$\sigma_{diff}^2 = N_+ + \gamma^2 N_- \tag{8}$$

$$\mathrm{SNR}_{diff} = \frac{S_{diff}}{\sqrt{\sigma^2_{diff}}} = \frac{N_+ - \gamma N_-}{\sqrt{N_+ + \gamma^2 N_-}} \tag{9}$$

Three parameters can be used to define the shape of the differential pinhole projection defined in equation (7): α, the ratio of the outer to the inner pinhole radius; γ, the multiplication factor applied to the photon count from the outer annulus; and r_i, the inner pinhole radius. This paper is concerned with the optimum choice of these parameters to give a good resolution whilst maintaining a good SNR. It is useful to see how variations in these parameters affect the point-spread functions. Figures 3(a) and 3(c) show the effect of changing α on the lateral confocal point-spread function. It may be seen that as α is increased the PSF mainlobe width reduces but at the expense of negative sidelobes. A similar pattern of PSF changes is observed in figure 3(c) when the multiplication factor is increased.

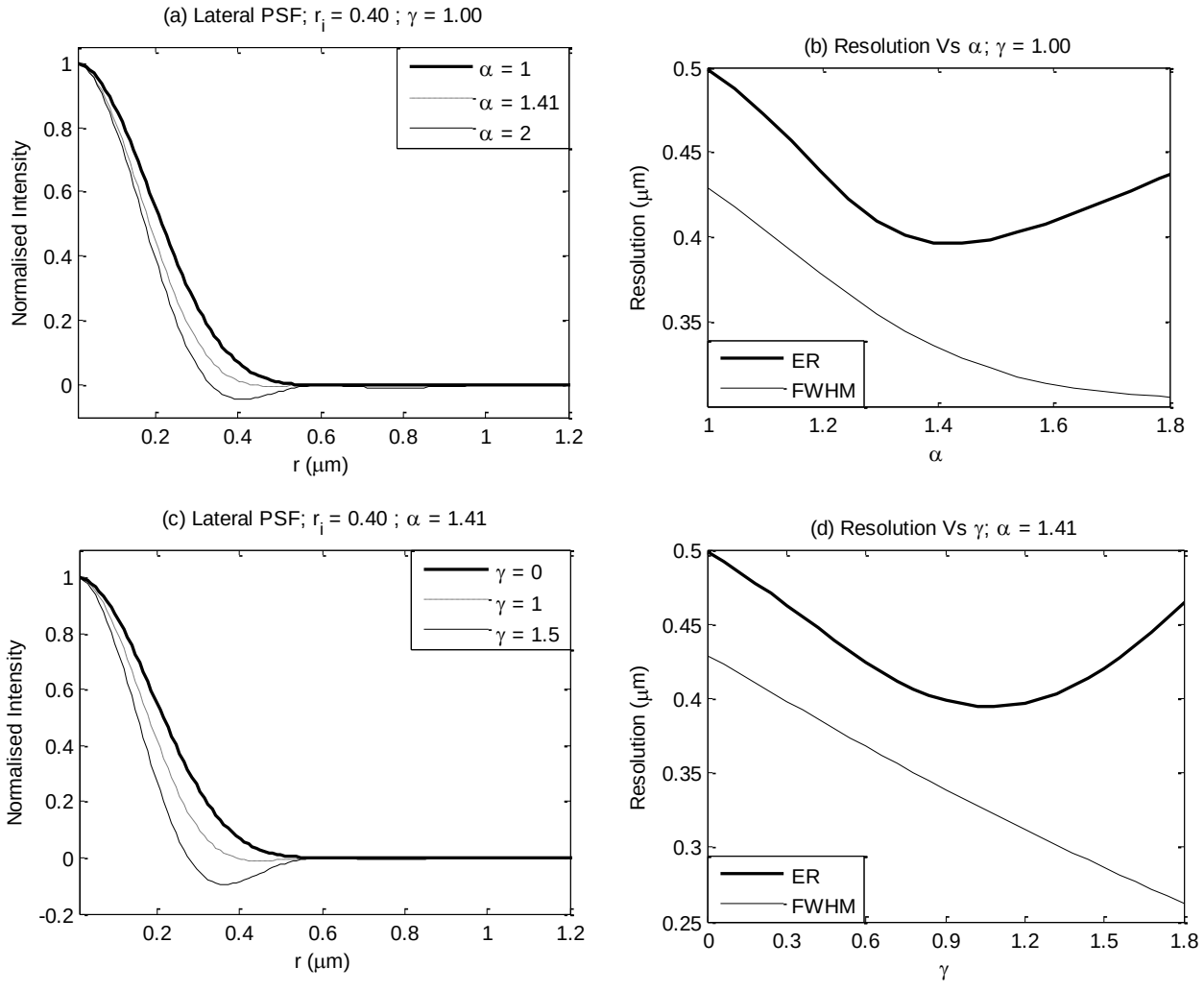

Figure 3. Effect of varying $\boldsymbol{\alpha}$ and $\boldsymbol{\gamma}$ on the lateral responses of a confocal fluorescence microscope employing a differential pinhole. Similar trends can be observed for the axial responses and thus not shown here. Note how the negative sidelobes produced on increasing $\boldsymbol{\alpha}$ or $\boldsymbol{\gamma}$ is accounted for only by the ER metric. Here $\boldsymbol{r_i = 0.4\mu m}$, NA = 0.5 and $\boldsymbol{\lambda}$ = 0.5μm

A commonly used measure of the resolution of an optical system is the width of the PSF as characterised by the full-width at half maximum (FWHM). The FWHM observed as α and γ are increased are plotted as the thinner lines in figures 3(b) and 3(d), respectively. It may be seen that, by this measure, the resolution appears to improve as α and γ are increased. However, clearly, this measure does

not take into account the presence of the increasing negative sidelobes visible in figures 3(a) and 3(c). In order to take account of the negative effect of such sidelobes on imaging performance, we shall use an alternative measure of resolution designated as equivalent radius (ER). For lateral resolution the ER is defined as the radius of a circular top-hat function with a height of the maximum of the PSF and with the same volume as the modulus of the PSF. For the axial resolution ER is defined as the radius of a top-hat function with the height of the maximum of the axial response and with the same area as the modulus of the axial response. Mathematically, ER in the lateral direction ER_{lat} and axial direction ER_{ax} can be calculated as, in equations (10) and (11) respectively,

$$ER_{lat} = \sqrt{2\int |PSF(v)|vdv} \tag{10}$$

$$ER_{ax} = \int |PSF(u)|du \tag{11}$$

and importantly, these measures take into account the presence of side lobes in the PSFs. These ER measures are plotted as the bolder lines in figures 3(b) and 3(d) and it may the seen that as α and γ increase the ER resolutions initially improve as the main lobe narrows but then deteriorate as the effect of the negative sidelobes increases.

As the pinhole geometry is controlled by three parameters and the result of changing any of these parameters will, influence both the resolution and the SNR of the system; it is a complex task to try to find optimum conditions. To constrain the problem, we have imposed a constraint of always varying r_i to generate a chosen SNR value. This value we have set at 0.5; this means that the differential pinhole with selected α and γ values is assumed to be adjusted in overall radius so as to deliver a SNR of 0.5 (i.e. the same SNR as for a conventional confocal pinhole that admits 25% of the image-plane light). Constrained in this way, the resolution achievable for any α and γ values can be found. These are plotted (as contour diagrams) for the lateral and axial (ER) resolutions in figures 4(a) and 4(b).

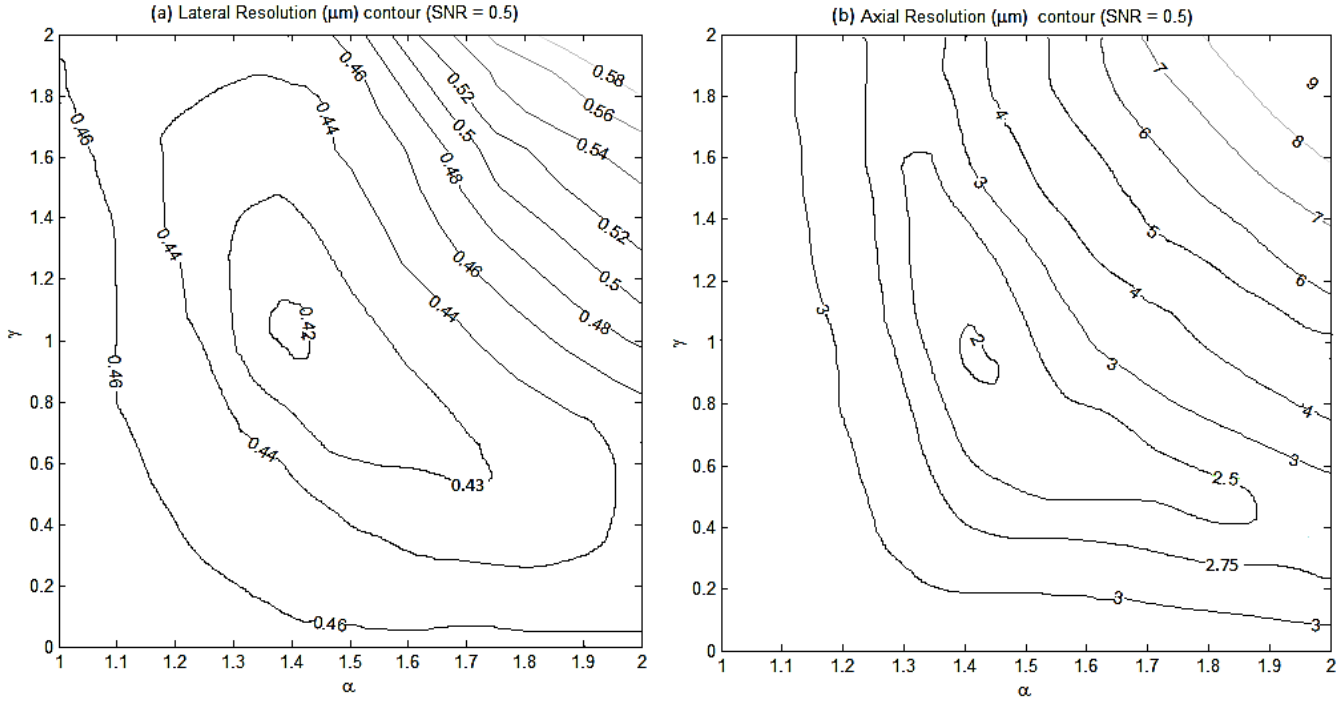

Figure 4. ER based resolution contours for a constant SNR of 0.5. Minimas of the respective contours are found to be at $\boldsymbol{\alpha}$ = 1.41 and $\boldsymbol{\gamma}$ = 1.00. Here NA = 0.5 and $\boldsymbol{\lambda}$ = 0.5 μm

It may be seen, that in both the lateral and axial cases, a minimum is present in these plots, indicating that an optimum pairing of α and γ exists. It is convenient that the optimum positions in both plots are closely aligned at around the $\alpha = 1.41$ and $\gamma = 1$ positions. Similar plots for different SNR values (below about 0.63) also show minima in these positions. This suggests that these values can be regarded as optimum in designing a differential pinhole. It is also interesting to examine the performance of a differential pinhole with these parameters by plotting, the type of resolution vs SNR characteristic plot shown in figure 2 and to compare with the plot for a conventional confocal pinhole. Figure 5 shows examples of these plots for the lateral and axial cases plotted both for the FWHM and the ER resolution criteria.

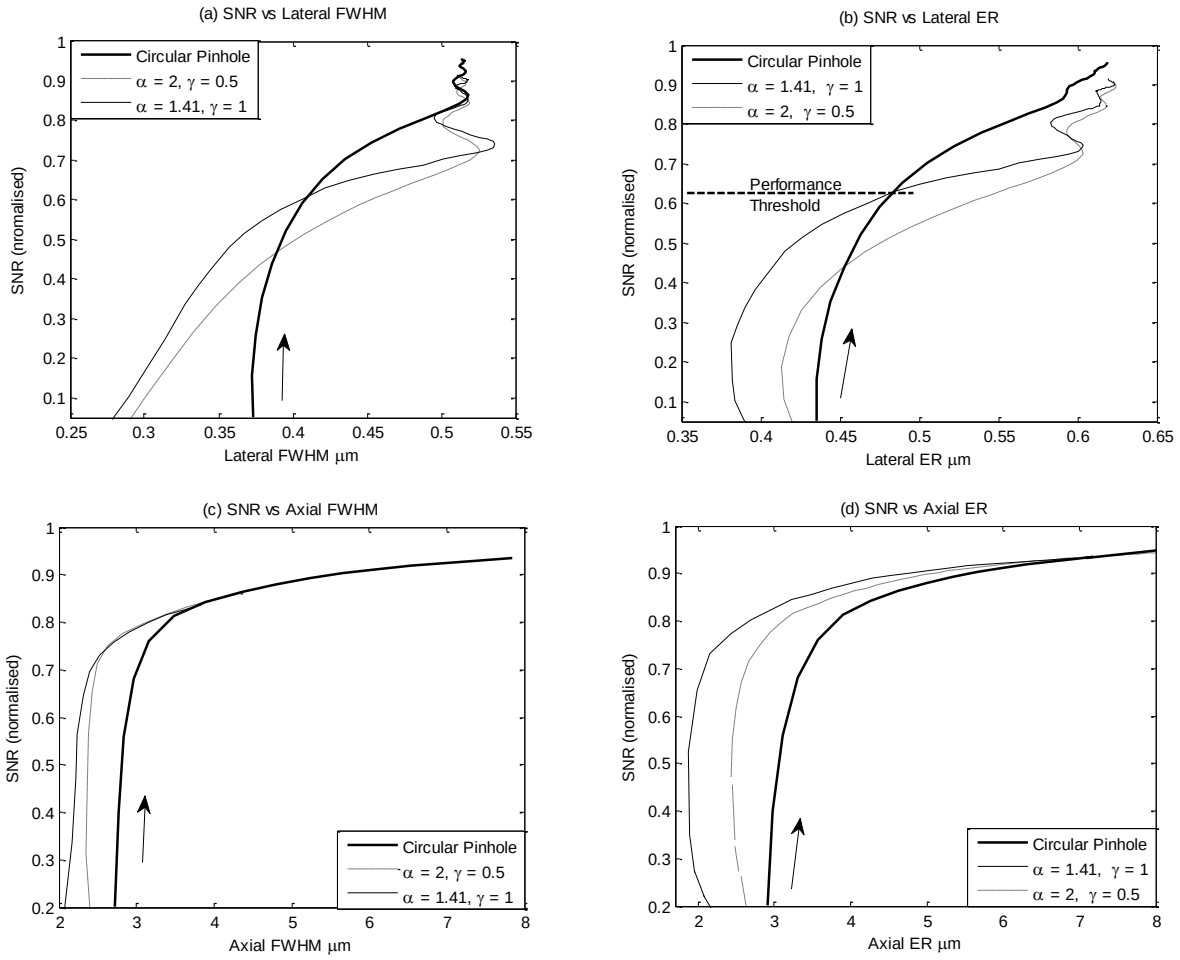

Figure 5. SNR Vs resolution characteristics based on FWHM (plots (a) and (c)) and ER (plots (b) and (d)). Arrows indicate direction of increasing r_i.

The bold dashed line in figure 5(b) marks the SNR threshold of 0.63 beyond which the differential pinhole based CFM system underperforms (worse SNR-resolution trade-off) with respect to a conventional (circular pinhole based) CFM system in the lateral direction. Below this threshold, the differential pinhole based CFM system offers maximum and simultaneous 3D resolution gains over conventional (circular pinhole based). This is realised with parameters $\alpha = 1.41$ and $\gamma = 1.00$. For any other parameter set chosen, the SNR of the differential pinhole system will always result in a lower SNR value than a conventional CFM system. However, it can be seen from figure 5(d), that the differential pinhole system outperforms (better SNR-resolution trade-off) the conventional system, with the optimum parameter set, in the axial direction for all SNR values. It should be noted that the graphs presented in figure 5 are

calculated for NA = 0.5 and for $\lambda = 0.5\mu m$. However the threshold value of 0.63 quoted for these parameters does not change significantly for different parameters. For example for NA = 0.7 and $\lambda = 0.4\mu m$, the threshold value changes to around 0.61.

4. Image Simulation Results

To further illustrate the potential advantage of employing a differential pinhole system, computer simulated images have been generated to show the imaging performance predicted for some simple object forms. The images presented in this section have been generated using the commonly-used paraxial and scalar imaging approximations [33], which allow the use of discrete Fourier transforms to convert pixelated representations of pupil functions to point-spread functions; convolution operations were also implemented through Fourier transformation, multiplication and inverse transformation using the *fft2* function in MATLAB. The accuracy of the use of a Fourier optics approach has been discussed by a number of authors, see for example [34, 35]. Shot noise was modelled using the MATLAB Poisson noise generator *poissrnd*.

Figure 6 plots the absolute values of simulated images of an annular object as imaged by a circular pinhole CFM system (pinhole radius = 0.4μm) and a differential pinhole (circular projection of which has an outer pinhole radius 0.6μm, $\alpha = 1.41$ and $\gamma = 1$), with radii chosen to give the same SNR in both cases. The images have been generated by convolving the 2D object function with the 2D confocal PSF in the plane of focus. Although absolute values are displayed in figure 6, as the total PSF negative dip intensity is small, virtually identical images would be observed by just displaying the positive image intensities. The resolution improvement can be clearly observed here.

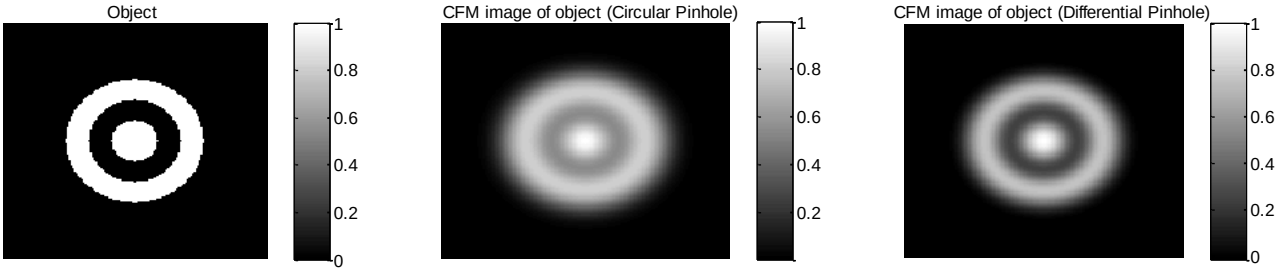

Figure 6. Comparing the CFM image of an annular object using a circular and differential pinhole at an outer pinhole radius of 0.4μm and 0.6μm respectively. Object consists of two fluorescent rings of width 0.5μ**m** separated by the same distance.

In figure 7, two planar objects are imaged – one an annular ring structure placed at z = 0 and the second a cross placed at z = 4μm. Both the fluorescent objects have been normalised so that each emits the same mean number of photons for equal uniform illumination. Shown are a series of sectioned images as the focal plane of the illumination is moved between the two object planes. Owing to the tighter PSF mainlobe width and negligible negative sidelobes, the differential pinhole (circular projection of which has an outer pinhole radius 0.6μm, $\alpha = 1.41$ and $\gamma = 1$) based system compared to its circular pinhole counterpart (outer pinhole radius 0.4μm, $\alpha = 1$and $\gamma = 0$) shows a greater separation of the two objects e.g. in the second image from the left in the top row the cross is still clearly visible in this image but in the lower image the cross is nearly invisible.

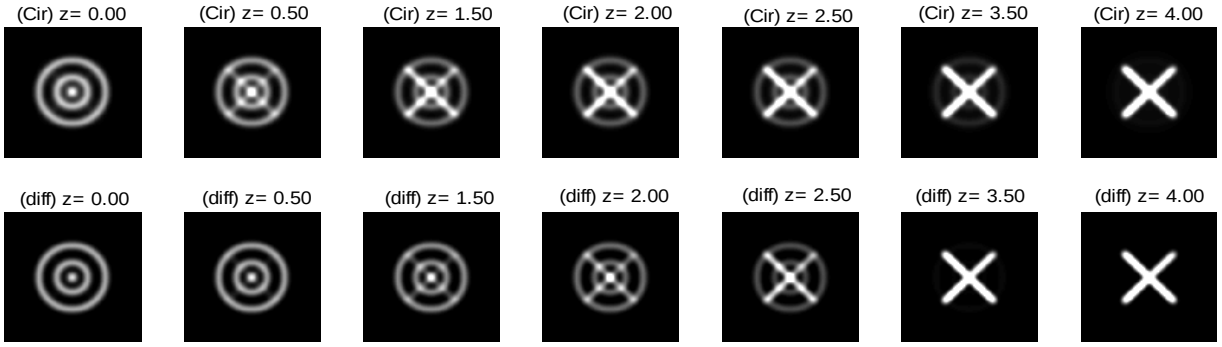

Figure 7. CFM images of an annular ring (located at z=0 plane) and a cross shaped object (located at z=4μm plane) for an SNR of 0.5 using a circular pinhole (top row) with r_p= 0.4μm and a differential pinhole (bottom row) with r_p = 0.6μm. The annular ring object consists of three concentric rings of width 0.3μm separated by 1 μm.The width of lines in the cross shaped object is 0.3μm.

5. Conclusions

In this paper an optimum profile for the circular projection of an elliptically shaped differential pinhole has been deduced through the introduction of a new resolution metric, equivalent radius, which overcomes the inability of the conventional FWHM to take into account sidelobes in the PSF. For SNR < 0.63 it has been shown that simultaneous resolution gains over a conventional circular pinhole geometry based CFM system, along both the lateral and axial directions can be obtained by setting the parameters α = 1.41 and γ = 1 for the differential pinhole. In regard to the SNR-axial resolution trade-off, the differential pinhole system outperforms the conventional system, with the optimum parameter set, for all SNRs values. Requiring no significant modification to the CFM setup and using fast point detectors, the now optimised differential pinhole detection based CFM system offers significant 3D resolution gains at SNR < 0.63. Although the new system carries a slightly increased overall implementation cost over a conventional circular pinhole geometry CFM system, the results show that images of considerably higher quality are produced.

References

1. Lipson, S.G., *Why is super resolution so inefficient?* Micron, 2003. **34**: p. 309-312.
2. Hayat, M.A., *Principles and techniques of electron microscopy: biological applications*. 4th ed. 2000: Cambridge University Press.
3. Heintzmann, R. and G. Ficz, *Breaking the resolution limit in light microscopy.* Briefings in Functional Genomics and Proteomics, 2006. **5**(4): p. 289-301.
4. Garini, Y., B.J. vermolen, and I.T. Young, *From micro to nano: recent advances in high-resolution microscopy.* Current Opinion in Biotechnology, 2005. **16**: p. 3-12.
5. Kam, Z., B. Hanser, M.G.L. Gustafsson, D.A. Agard, and J.W. Sedat. *Computational adaptive optics for live three-dimensional biological imaging*. in *Proceeding in National Academy of Science* 2000.
6. Schermelleh, L., R. Heintzmann, and H. Leonhardt, *A guide to super-resolution fluorescence microscopy.* The Journal of Cell Biology, 2010. **190**(2): p. 165-175.
7. Beweresdorf, J., R. Schimdt, and S.W. Hell, *Comparison of I5M and 4Pi-microscopy.* Journal of Microscopy, 2006. **222**(2): p. 105-117.
8. Fernandez-suarez, M. and A.Y. Ting, *Fluoroscent probes for super-resolving resolution imaging in living cells*, in *Nature*. 2008. p. 929-943.

9. Bailey, B., D.L. Farka, D.L. Taylor, and F. Lanni, *Enhancement of axial resolution in fluorescence microscopy by standing-wave excitation.* Nature, 1993. **366**(44-48).
10. Gustafsson, M.G.L., *Surpassing the lateral resolution limit by a factor of two using structured illumination microscopy.* Journal of Microscopy, 2000. **198**: p. 82-87.
11. Heintzamnn, R. and C.G. Cremer. *Laterally modulated excitation microscopy: improvement of resolution by using a diffraction grating*. in *Optical Biopsies and Microscopic Technqiues III*. 1999. SPIE.
12. Fedossev, R., Y. Belyaev, J. Frohn, and A. Stemmer, *Structured light illumination for extended resolution in fluorescence microscopy.* Optics and Lasers in Engineering, 2005. **43**(3): p. 403-414.
13. Frohn, J.T., H.F. Knapp, and A. Stemmer, *True optical resolution beond the Rayleigh limit achieved by standing wave illumination*. 2000, National Academy of science: USA. p. 7232-7236.
14. Heintzmann, R., *Saturated patterned excitation microscopy with two-dimensional excitation patterns.* Micron, 2003. **34**: p. 283-291.
15. Wabuyele, M.B., M. Culha, G.D. Griffin, P.M. Viallet, and T. Vo-Dinh, *Near-Field Scanning Optical Microscopy for Bioanalysis at Nanometer Resolution*. Protein Nanotechnology 2005: Springer.
16. Huang, B., W. Wang, M. Bates, and X. Zhuang, *Three-dimensional super-resolution imaging by stochastic optical reconstruction microscopy.* Science, 2008. **319**: p. 810-813.
17. Somekh, M.G., K. Hsu, and M.C. Pitter, *Resolution in structured illumination microscopy.* Optical Society of America, 2008. **25**(6): p. 1319-1329.
18. Somekh, M.G., K. Hsu, and M.C. Pitter, *Effect of processing strategies on the stochastic transfer function in structured illumination micrscopy.* Optical Society of America, 2011. **28**(9): p. 1925-1934.
19. Heintzmann, R., V. Sarafis, P. Munroe, J. Nailon, Q.S. Hailey, and T.M. Jovin, *Resolution enhancement by subtraction of confocal signals takes at different pinhole sizes.* Micron, 2003. **34**(6): p. 293-300.
20. Wang, Y., C. Kuang, Z. Gu, and X. Liu, *Image subtraction method for improving lateral resolution and SNR in confocal microscopy.* Optics and Lasers Technology, 2012. **48**: p. 489-494.
21. Martinez-Corral, M., M.T. Caballero, C. Ibanez-Lopez, and V. Sarafis, *Optical sectioning by two pinhole confocal fluorescence microscopy.* Micron, 2003. **34**(6-7): p. 313-318.
22. Ortiga, E.S., C.J.R. Sheppard, G. Saavedra, M. Martinez-Corral, A. Doblas, and A. Calatayud, *Subtractive imaging in confocal scanning microscopy using a CCD camera as a detector.* Optics Letters, 2012. **37**(7): p. 1280-1282.
23. Segawa, S., Y. Kozawa, and S. Sato, *Resolution enhancement of confocal micrsocopy by subtraction method with vector beams.* Optics Letters, 2014. **39**(11): p. 3118-3121.
24. Gu, M., *Principles of Three Dimensional Imaging in Confocal microscopes*. 1996: World Scientific. 337.
25. Born, M. and E. Wolf, *Priciples of Optics*. 1993: Cambridge University Press.
26. Sheppard, C.J.R., *Limitations of paraxial Debye approximation.* Optics Letters, 2013. **38**(7): p. 1074-1076.
27. Sheppard, C.J.R. and T. Wilson, *Image formation in confocal scanning microscopes.* Optik, 1980. **55**(4): p. 331-342.
28. Somekh, M.G., K. Hsu, and M.C. Pitter, *Stochastic transfer function for structured illumination microscopy.* Optical Society of America, 2009. **26**(7): p. 1630-1637.
29. Becker, W., et al. *High-speed FLIM data acquisition by time-correlated single-photon counting*. in *Multiphoton Microscopy in the Biomedical Sciences IV*. 2004. San Jose, CA: SPIE Proceedings.
30. Bertero, M., P. Boccacci, M. Defrise, C.D. Mol, and E.R. Pike, *Super-resolution in confocal scanning microscopy: II. The incoherent case.* Inverse Problems, 1989. **5**: p. 441-461.
31. Sheppard, C.J.R., *Super-resolution in Confocal Imaging.* Optik, 1988. **80**(2): p. 53-54.

32. Huff, J., W. Bathe, R. Netz, T. Anhut, and K. Weisshart *The Airyscan Detector from ZEISS Confocal Imaging with Improved Signal-to-noise Ratio and Superresolution*. Carl Zeiss Microscopy Technical Note, 2015.
33. Goodman, J.W., *Introduction to Fourier Optics*. 2005: Roberts & Company.
34. Stamnes, J.J., *Computation of Focused Fields*, in *Waves in Focal Regions: Propagation, Diffraction and Focusing of Light, Sound and Water Waves*. 1986, Taylor & Francis.
35. Qi, F., V. Tavakol, D. Schreurs, and B. Nauwelaers, *Limitations of Approximations towards Fourier Optics for indoor active millimeter wave imaging systems.* Progress in Electromagnetics Research, 2010. **109**: p. 245-262.